Two-dimensional optical spatiotemporal solitons in quadratic media

Xiang Liu, Kale Beckwitt, and Frank Wise
Department of Applied Physics, Cornell University, Ithaca, New York 14853
(Received 24 January 2000)

Numerical and experimental studies of the propagation of femtosecond-duration optical pulses in quadratic nonlinear media are presented. Pulse evolution is investigated over wide ranges of initial intensity and phase mismatch between fundamental and harmonic waves, and the conditions that produce two-dimensional spatiotemporal solitons are delineated. Spatiotemporal solitons can be generated when the group velocities of the fundamental and harmonic fields are quite different, for proper choice of the phase mismatch. The factors that limit the formation of spatiotemporal solitons are discussed.

PACS number(s): 42.65.Tg

I. INTRODUCTION

Optical solitons are localized electromagnetic waves that propagate steadily in nonlinear media with group-velocity dispersion (GVD), diffraction, or both. Temporal solitons in single-mode optical fibers are the prototypical optical solitons; these were predicted in 1973 [1] and first observed in 1980 [2]. It has long been understood that self-focusing as a result of the cubic ($\chi^{(3)}$) Kerr nonlinearity could compensate for the spreading of a beam due to diffraction, but the resulting balance is unstable in greater than one dimension [3]. Spatial solitons were first produced in liquid CS_2, where an interference grating was employed to stabilize the solitons [4], and light filaments were observed [5] in resonant propagation through an atomic vapor, where the nonlinearity is saturable. One-dimensional (1D) spatial solitons of the nonlinear Schrödinger equation were generated in a glass waveguide in 1990 [6].

In the last decade, two new nonlinear-optical interactions that support solitons were discovered. Segev *et al.* [7] predicted that the photorefractive effect in electro-optic materials could be used to create a saturable nonlinear index of refraction, and photorefractive solitons were observed soon afterward [8]. At nearly the same time, there was a resurgence of interest [9–11] in the effective cubic nonlinearity that is produced by the cascaded interactions of two or three waves in quadratic ($\chi^{(2)}$) nonlinear media. The renewed interest was based on the recognition that large nonlinearities of controllable sign can be produced. The cascade nonlinearity saturates with intensity, so self-focusing collapse can be avoided in quadratic media [12]. Numerous theoretical treatments of solitons in quadratic media have been reported [13–25]. On the experimental side, Torruellas *et al.* succeeded in generating stationary two-dimensional spatial solitons in 1995 [26], and Di Trapani and co-workers recently produced temporal solitons via the cascade nonlinearity [27].

Photorefractive and quadratic solitons are fundamentally different from 1D solitons in Kerr media because they are modeled by nonintegrable systems. Higher dimensional solitons in Kerr media are also modeled by nonintegrable systems. Strictly speaking, stable self-trapped beams and pulses in saturable Kerr and quadratic media should be referred to as ''solitary waves,'' but following common usage, we will refer to them as ''solitons.'' In quadratic media, the soliton actually consists of two fields at different frequencies, coupled and mutually trapped by the nonlinear interaction.

One of the major goals in the field of soliton physics is the production of pulses of light that are localized in space and time, i.e., spatiotemporal solitons (STS's). It is well-known that STS's are unstable against collapse in cubic nonlinear media [28,29], but solutions may be stabilized if the nonlinearity is saturable or if additional nonlinear processes such as multiphoton ionization arrest the collapse favored by self-focusing. (In recent experiments the self-channeling of optical pulses in air has been observed [30]. We do not refer to these pulses as STS's because they do not result from a balance between nonlinearity and dispersion.) Several model systems capable of supporting STS have been analyzed theoretically [31–34]. Liu *et al.* recently reported the experimental generation of STS's: femtosecond pulses that overcome diffraction in one transverse spatial dimension as well as GVD to reach stable or periodically stable beam size and pulse duration were produced in the quadratic nonlinear crystal lithium iodate ($LiIO_3$) [35]. We will refer to these as 2D STS, to distinguish them from pulses localized in all three dimensions and therefore referred to as three-dimensional (3D) STS. $LiIO_3$ was chosen for the initial experiments largely because it is possible to match the group velocities of pulses at the fundamental (FH) and second-harmonic (SH) frequencies in this material. Group-velocity mismatch (GVM) tends to reduce and distort the nonlinear phase shift produced in the cascade process. In addition, GVM naturally counters the mutual trapping of FH and SH fields that occurs in quadratic solitons.

Here we provide a more systematic description of the experiments on STS's with nearly zero GVM than was possible in the brief initial report [35]. We also present the results of a study of STS's in the presence of significant GVM, performed with barium metaborate (Ba_2BO_4 or BBO) as the quadratic medium. The ranges of parameters for which STS's can be produced are delimited experimentally. The paper is organized as follows. In Sec. II we introduce the basic theoretical background and the coupled wave equations. Section III describes the experimental apparatus and issues. Section IV describes STS observed with nearly matched group velocities, and Sec. V deals with the case of significant GVM. The stability map will be presented in Sec. VI. Our conclusions are summarized in Sec. VII.

II. PULSE PROPAGATION IN QUADRATIC MEDIA

Within the slowly varying envelope approximation, the equations that govern the interaction of FH and SH electric fields (E_1 and E_2, respectively) propagating in the z direction (and assumed constant in the x direction) in a medium with quadratic and cubic nonlinearity are

$$\left(\frac{\partial}{\partial z}+\frac{iZ_I}{4L_{\mathrm{DS1}}}\frac{\partial^2}{\partial t^2}+\frac{iZ_I}{4L_{\mathrm{DF1}}}\frac{\partial^2}{\partial y^2}\right)E_1 = iE_1^*E_2e^{i\Delta kz}+i2\pi(n_2I_0)\frac{Z_I}{\lambda}(|E_1|^2+\tfrac{2}{3}|E_2|^2)E_1,$$
$$\left(\frac{\partial}{\partial z}+\frac{iZ_I}{L_{\mathrm{GVM}}}\frac{\partial}{\partial t}+\frac{iZ_I}{4L_{\mathrm{DS2}}}\frac{\partial^2}{\partial t^2}+\frac{iZ_I}{4L_{\mathrm{DF2}}}\frac{\partial^2}{\partial y^2}\right)E_2 = iE_1E_1e^{-i\Delta kz}+i4\pi(n_2I_0)\frac{Z_I}{\lambda}(\tfrac{2}{3}|E_1|^2+|E_2|^2)E_2. \quad (1)$$

E_1 and E_2 are in units of the initial peak FH field E_0 (related to the initial peak FH intensity by $I_0=\sqrt{\varepsilon/\mu}|E_0|^2/2$), n_2 is the Kerr nonlinear index, and $\Delta k=k_{2\omega}-2k_{\omega}$ is the wave-vector mismatch between fundamental and harmonic fields. The diffraction, dispersion, and nonlinear lengths characterizing the pulse propagation are $L_{\mathrm{DF}}=k\omega_0^2/2$, $L_{\mathrm{DS}}=0.322\tau_0^2/|\beta^{(2)}|$, and L_{NL} (the length over which the accumulated nonlinear phase shift is 1), respectively, where λ is the FH wavelength. The normalizing length $Z_I=n\lambda/\pi\chi^{(2)}E_0$ characterizes the strength of the nonlinear coupling. Time t is measured in units of the initial pulse duration τ_0, and positions z and y are measured in units of L_{NL} and the y dimension beam waist ω_0, respectively. $\beta^{(2)}$ is the GVD, which will have contributions from both material dispersion and angular dispersion. The characteristic length over which the FH and SH pulses walk away from each other in time is $L_{\mathrm{GVM}}=c\tau_0/(n_{1g}-n_{2g})$ where n_{1g} and n_{2g} are the group indices at the FH and SH frequencies, respectively.

The large effective cubic nonlinearity in quadratic media results from the cascading of $\chi^{(2)}(2\omega;\omega;\omega)$ and $\chi^{(2)}(\omega;2\omega;-\omega)$ processes in phase-mismatched second-harmonic generation (SHG). The process of conversion and back conversion generates a nonlinear phase shift $\Delta\Phi^{\mathrm{NL}}$ at the FH frequency that is linear in intensity (at low intensities) and thus can be modeled as an effective nonlinear refractive index $(n_2)_{\mathrm{eff}}$. [$\Delta\Phi^{\mathrm{NL}}$ normally refers to the maximum value of the time-dependent phase shift, but at times we will be concerned with the specific temporal variation $\Delta\Phi^{\mathrm{NL}}(t)$ across a pulse.] The SH field also acquires a nonlinear phase shift in the process. For large phase mismatch, low intensity, or both, the nonlinear phase shift can be approximated as $\Delta\Phi^{\mathrm{NL}}\approx-\Gamma^2L^2/\Delta kL$, where $\Gamma=d_{\mathrm{eff}}\omega|E_0|/c\sqrt{n_{\omega}n_{2\omega}}$ [11]. Depending on the sign of the phase-mismatch ΔkL, the phase shift can be either self-focussing ($\Delta kL<0$, $\Delta\Phi^{\mathrm{NL}}>0$) or self-defocusing ($\Delta kL>0$, $\Delta\Phi^{\mathrm{NL}}<0$).

Pulse propagation is modeled by numerically solving the propagation equations in one transverse spatial dimension and time. The equations are solved using a symmetric split-step beam-propagation method in which a fourth order Runge-Kutta algorithm solves the nonlinear propagation step in the time domain, and the dispersive and diffractive propagation steps are solved in the frequency domain. The numerical simulations use experimental parameters. The temporal profile and transverse intensity distribution of the initial FH pulse are taken as Gaussians. The results of the numerical solutions will be compared with experimental data below. All results are presented with time measured with respect to a reference frame moving at the group velocity of the FH pulse.

III. EXPERIMENTAL APPARATUS AND PARAMETERS

Solitons form when the effects of nonlinearity, diffraction, and dispersion balance each other, so the goal of the experimental arrangement is to match L_{DF}, L_{DS}, and L_{NL} at a length that is commensurate with available nonlinear crystals. BBO and $LiIO_3$ are the best commercially available crystals for 800→400 nm SHG, and it is difficult to obtain crystals longer than ~25 mm. Demonstration of soliton propagation requires propagation over at least ~3–5 characteristic lengths, which dictates characteristic lengths of a few mm. The focusing, pulse energy, and phase mismatch can be conveniently adjusted to produce L_{DF} and L_{NL} in this range. However, the GVD required to obtain $L_{\mathrm{DS}}\sim5$ mm with 100 fs pulses is an order of magnitude larger than that of most transparent materials. Adding to the difficulty is the fact that the GVD must be anomalous at both the FH and SH frequencies [33]. Thus, ordinary material dispersion is inappropriate for the generation of STS at visible or near-infrared wavelengths.

In general, angular dispersion of a light wave is accompanied by group-velocity dispersion. The large and anomalous GVD required to support solitons is produced by angular dispersion of the input pulse using a diffraction grating [36]. Different wavelengths in the pulse spectrum propagate at slightly different angles. As a consequence, the pulse front is tilted with respect to the propagation direction. Diffraction from a grating can also be used to match the group velocities of the FH and SH pulses; then each wavelength in the pulse spectrum propagates at its phase-matching angle. This is referred to as achromatic phase matching (APM). APM is a well known technique in the ultrafast nonlinear optics field for efficient wavelength conversion. Each fundamental wavelength is phase matched with its own SH, so the phase-matching bandwidth as compared to ordinary SHG is greatly increased. Equivalently, the FH-SH GVM is substantially reduced. APM was recently used for generation of 1D temporal solitons [27,37]. Using APM, the effective GVD and GVM cannot be chosen independently. Regardless of whether the GVD is produced by angular or material dispersion, the GVD at the FH and SH frequencies will generally differ. Thus, the shape of STS will not have spatiotemporal rotation symmetry, but will be elliptical [38].

The experimental apparatus [Fig. 1(a)] is similar to that described in [35]. A Ti-sapphire regenerative amplifier produces pulses of duration 120 fs and energy up to 1 mJ at a wavelength of ~800 nm. The incoming pulses diffract off a grating and pass though a 1:1 telescope and a cylindrical lens prior to incidence on the SHG crystal ($LiIO_3$ or BBO, cut for type-I interaction). The grating creates large and negative

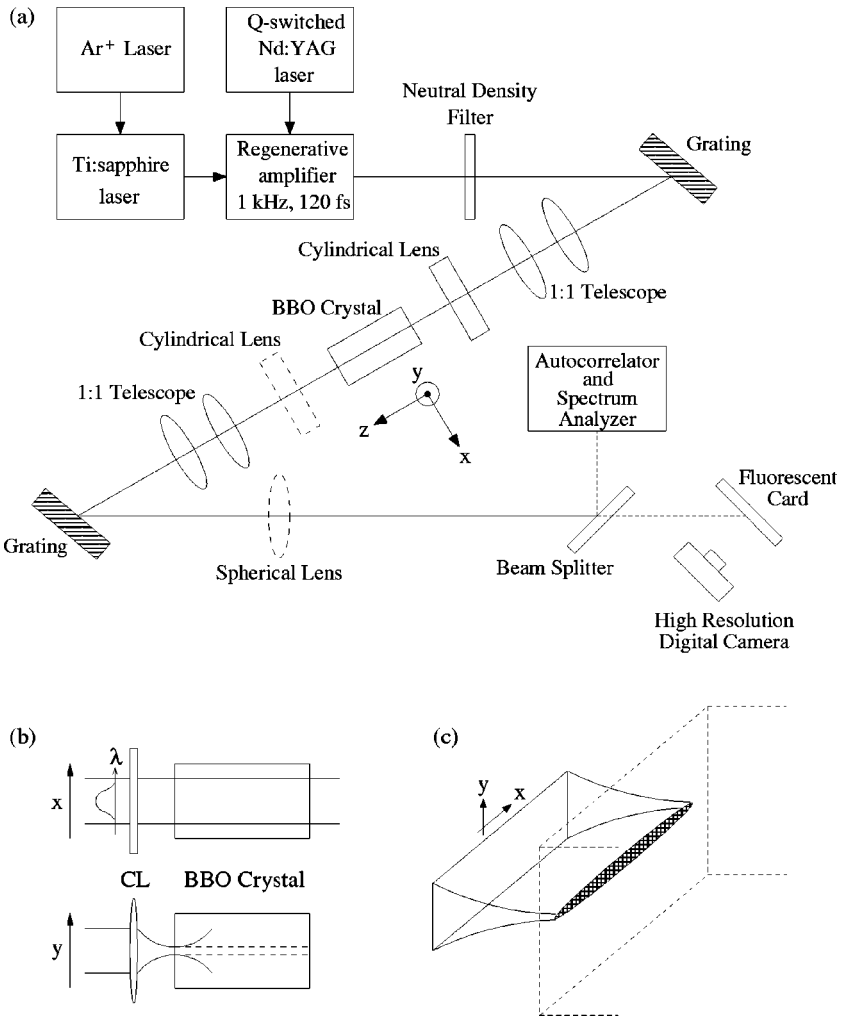

FIG. 1. Experimental apparatus (a). Schematic of the experiment (b) and (c). Propagation is along *z*, different wavelengths are dispersed along *x*. A cylindrical lens (CL) focuses the beam in y. The dashed lines indicate beam propagation for STS formation.

GVD by dispersing the spectrum in the horizontal transverse (*x*) direction [Fig. 1(b)]. The cylindrical lens focuses the beam in the *y* direction [Figs. 1(b) and 1(c)]. The beam waist in the unfocused (*x*) direction is 3–4 mm, so diffraction is negligible in that direction. Following the crystal, the optics are repeated in reverse order to undo the dispersion imposed by the grating and to collimate the beam. To image the beam at the exit face of the crystal, the second cylindrical lens is removed, and the beam is imaged with a spherical lens following the second grating.

In our experiment angular dispersion of $\sim 0.05°/\mathrm{nm}$ is required to achieve the desired GVD. In the absence of nonlinearity, this angular dispersion will broaden the pulse in the *x* direction by $\sim 100\ \mu\mathrm{m/cm}$, which is negligible compared to the initial *x* dimension beam size. However, spatial broadening due to angular dispersion can have a large effect if it is on the order of the *x* dimension beam size; this will be pertinent to the discussion of instabilities in Sec. VI.

The duration and spectrum of the FH pulse are measured with a background-free autocorrelator and diode-array spectrometer. The FH and SH beams are measured by imaging the exit face of the nonlinear crystal onto a charge-coupled device camera, or onto a card to be photographed with a high-resolution digital camera. Cross sections of the beam profiles are obtained from the two-dimensional digital images.

The clearest experimental evidence of soliton formation would consist of measurements of the spatial and temporal profiles of the pulse obtained at many different propagation distances. For temporal solitons in fibers, this is conveniently accomplished by cutting the fiber. Such an approach is difficult with STS's in quadratic media. As mentioned above, the longest readily available crystals offer ~ 5 characteristic lengths of propagation. One to two characteristic lengths may be needed for the launched pulse to evolve to a soliton, so solitons can be observed over the limited range of ~ 3–5 characteristic lengths. With two crystals, evolution over ~ 8 characteristic lengths can be observed. We will present measurements made at one or two different propagation distances in this range. Given the practical constraint on propagation distance, we rely on the variation of the output pulse with intensity and phase mismatch (at fixed propagation distance) to augment the limited direct measurements of pulse propagation.

IV. SPATIOTEMPORAL SOLITONS GVM NEAR ZERO

Group-velocity mismatch (and its spatial analog, walkoff) between the FH and SH pulses will limit conversion and back-conversion efficiency, which in turn limit the phase shift attainable with the cascade process. In addition, GVM distorts the temporal variation of $\Delta\Phi^{\mathrm{NL}}(t)$ from the shape produced by the electronic Kerr effect, namely, $\Delta\Phi^{\mathrm{NL}}(t) \sim I(t)$ [10,39–41]. One might expect that GVM can prevent

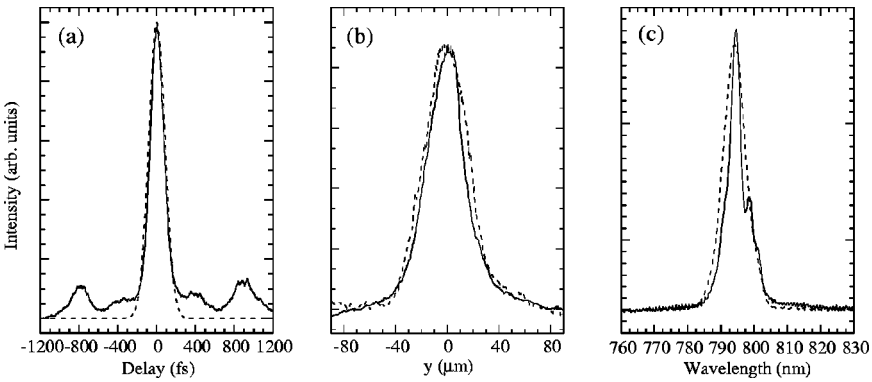

FIG. 2. Temporal (a), spatial (b), and spectral (c) profiles of FH pulses at exit face of 10 mm $LiIO_3$ with $I \approx 11$ GW/cm^2 and $\Delta kL = -30\pi$. Dashed lines indicate the input profiles.

the formation of STS's by splitting the coupled FH and SH pulses before mutual trapping can take effect [27]. Given these concerns, we first designed experiments on STS formation with nearly zero GVM.

If we arrange the pulse tilt to establish zero GVM in BBO, L_{DS} at the FH frequency will be at least 9 mm, which is too long for STS experiments. In $LiIO_3$, nearly zero GVM can be obtained simultaneously with $L_{DS} \approx 2$ mm, so $LiIO_3$ was chosen for these experiments. A diffraction grating with 1400 lines/mm and an incident angle of 20° produces net anomalous GVD of magnitude $|\beta^{(2)}| \approx 2400$ fs^2 (1200 fs^2) at the FH (SH) frequency in $LiIO_3$. Including the material dispersion of $LiIO_3$, the total FH (SH) dispersion is -2200 fs^2/mm (-600 fs^2/mm). To realize perfect GVM cancellation, the experimental parameters must be very precisely controlled. However, numerical simulations show that a slight deviation from perfect GVM compensation ($\lesssim 20\% \tau_0$ temporal walkoff per soliton period) does not significantly alter the formation of STS. This contrasts with the case discussed in Sec. V, where the large effect of GVM causes temporal walking of $\sim \tau_0$ per soliton period. A Gaussian beam waist of 40 μm (full width at half maximum) in the y direction produces $L_{DF} \approx 3$ mm, nearly matching L_{DS}. Ideally, we would have L_{DF} and L_{DS} matched for both FH and SH pulses. Experimentally, this is not feasible, but we found in both experiment and numerical simulation that robust STS are formed with up to ~40% mismatch between L_{DF} and L_{DS}. Intuitively, this can be understood as the STS adjusting its spatiotemporal profile to match L_{DF} and L_{DS} after some propagation. A 10-mm $LiIO_3$ crystal provides over three characteristic lengths of propagation. Control experiments confirm that STS's cannot be formed without the appropriate cascade nonlinearity: at low intensity (less than ~1 GW/cm^2) or with the $LiIO_3$ crystal oriented to eliminate $\chi^{(2)}$ effects, dispersive and diffractive propagation is observed. With $\Delta kL > 0$, the cascade phase shift is negative (self-defocusing) and cancels the Kerr phase shift to some degree. Nonlinear dispersive propagation is observed, in good agreement with numerical simulations.

With the crystal oriented to produce self-focusing cascade phase shifts ($\Delta kL < 0$), the output pulse duration and beam profile depend on the incident intensity over a wide range of phase mismatch, $-300\pi < \Delta kL < -30\pi$. The pulse duration and beam waist begin to narrow (relative to the low-intensity values) when the intensity reaches ~1 GW/cm^2, indicating space-time focusing. At higher intensity the output pulse duration and beam profile essentially match those of the input pulse. For $\Delta kL = -30\pi$ (-80π) this occurs at $I_0 \approx 10$ GW/cm^2 (20 GW/cm^2) [35]. Typical experimental data are shown in Fig. 2, and numerical simulation of pulse propagation under these conditions (Fig. 3) shows that the pulse is stable after propagating ~1 characteristic length. The minimum phase mismatch is ultimately limited by spatial walkoff in the x-z plane to be $|\Delta kL| > 4\pi$ for an initial beam size of 2 mm in the x direction. However, uncertainties arising from the beam divergence, pulse chirp, and accuracy of the phase-matching angle restricted our experiments to the range $|\Delta kL| > (20 \pm 5)\pi$.

For slightly higher intensities, STS's are still formed, but the pulses are periodically stable. For example, Fig. 4 shows calculations with the same conditions as in Fig. 3, but with the intensity increased from 11 to 13 GW/cm^2. The period is ~17 mm. Experimentally, ~10% compression in both time and space is observed after 10 mm propagation. Thus, for a given phase mismatch, there is a fairly narrow range of intensity that will produce the truly stable STS. The soliton period naturally decreases with increasing nonlinear phase shift, i.e., with increasing intensity or decreasing phase mismatch. With the conditions of Fig. 4 but $I_0 = 20$ GW/cm^2, the soliton period is reduced to ~7 mm. Periodically stable STS's are obtained in numerical simulations for I_0 up to ~80 GW/cm^2 and $|\Delta kL|$ up to $\sim 100\pi$.

For intensities in the range 40–80 GW/cm^2, the experimental output pulse is significantly compressed in time and space compared to the input pulse. Compression by factors of 2 in time and 3 in space is illustrated by Figs. 2 and 3 of Ref. [35], for example. This compression is accompanied by the development of significant modulation of the pulse spectrum: with increasing intensity the spectrum becomes doubly, and then triply peaked. Calculations corresponding to $I_0 = 60$ GW/cm^2 (Fig. 5) show that the STS is periodically stable. The calculations are performed with the intensity somewhat smaller than in the experiment, to simulate the effect of a small loss due to two-photon absorption (TPA) at 400 nm (the SH frequency) in $LiIO_3$. The dramatic increases in intensity at $z \approx 8$ and ≈ 18 mm are probably damped or smoothed to some extent owing to TPA, but the agreement with experiment is nonetheless reasonable. Thus, we conclude that intensities ~5–8 times I_0 (0.3–0.6 TW/cm^2) are reached under these conditions. The TPA should help stabilize the pulse propagation at such high intensities, but obviously at the expense of pulse energy.

There are appreciable contributions to the total nonlinear phase shift from the Kerr nonlinearity in these experiments. The nonlinear index of refraction of $LiIO_3$ is fairly large; we

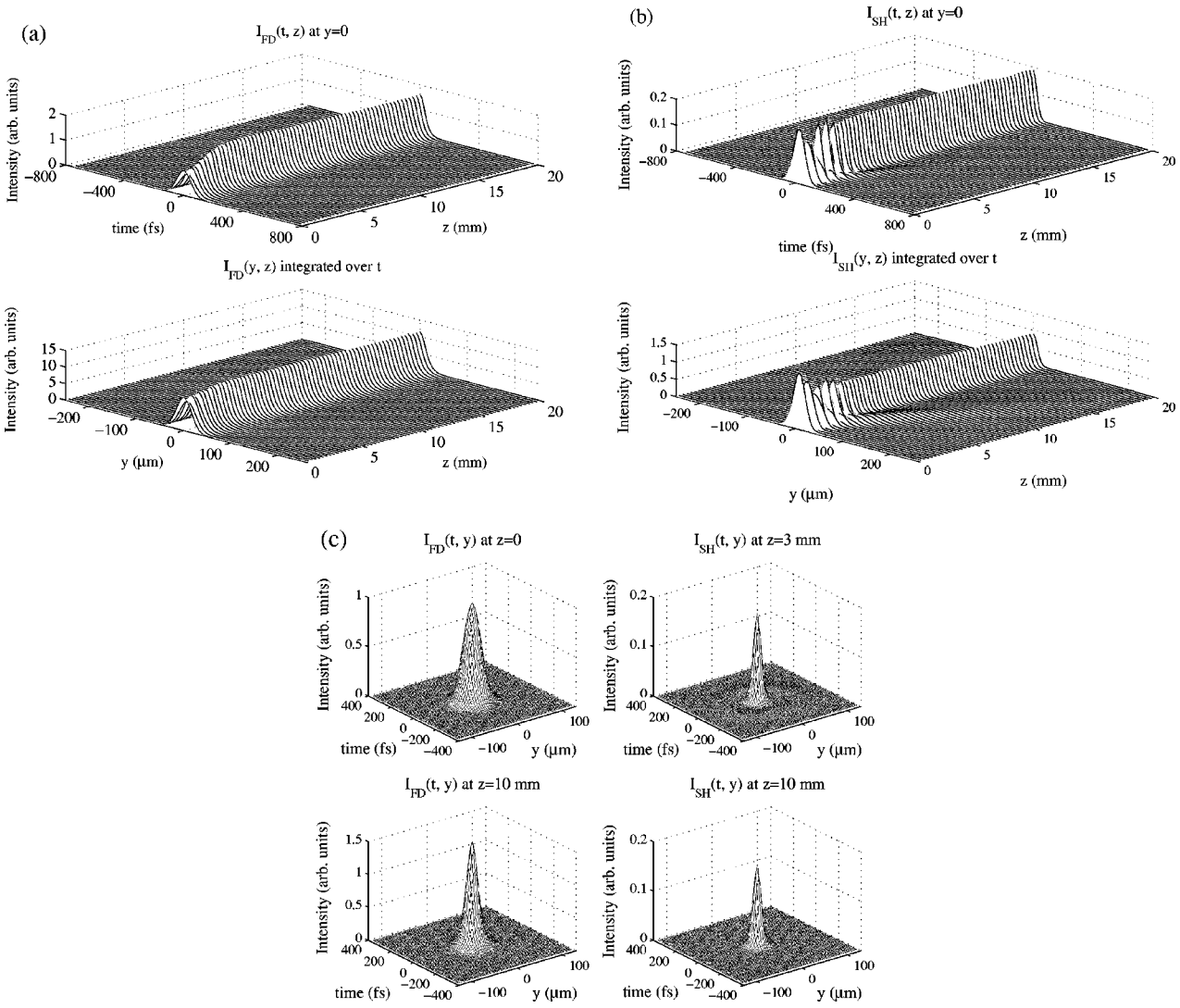

FIG. 3. Simulated FH (a) and SH (b) pulse propagation in $LiIO_3$ with $I=11$ GW/cm^2, $\Delta k=-30\pi/10$ mm, and GVM=0. The spatiotemporal profiles of the STS at different propagation lengths are shown in (c).

measure $n_2\approx 1\times 10^{-15}$ cm$^2/W$ using spectrally resolved two-beam coupling [42]. The corresponding critical power for self-focusing in one dimension is reached when $I_0\approx 80$ GW/cm^2. Information about the relative contributions of the cascade and Kerr nonlinearities is obtained from the threshold intensity for STS formation as well as the numerical simulations. The cascade phase shift varies from ~ 10 times the Kerr phase shift for $\Delta kL=-30\pi$ to $\sim$ equal to the Kerr phase shift when $\Delta kL=-200\pi$. Saturation of the cascade phase shift at high intensity is crucial to the stability of the STS. At large phase mismatch it is difficult to saturate the cascade nonlinearity, and this limits the formation of STS's.

V. PULSE PROPAGATION WITH GROUP-VELOCITY MISMATCH: WALKING SOLITONS

For analytic simplicity GVM is often neglected, in which case time and the transverse spatial coordinates are formally equivalent. However, quadratic solitons are fundamentally multiple-frequency entities. Thus, it is essential to establish the features that arise owing to GVM, as well as any restrictions that GVM imposes on the properties of the STS.

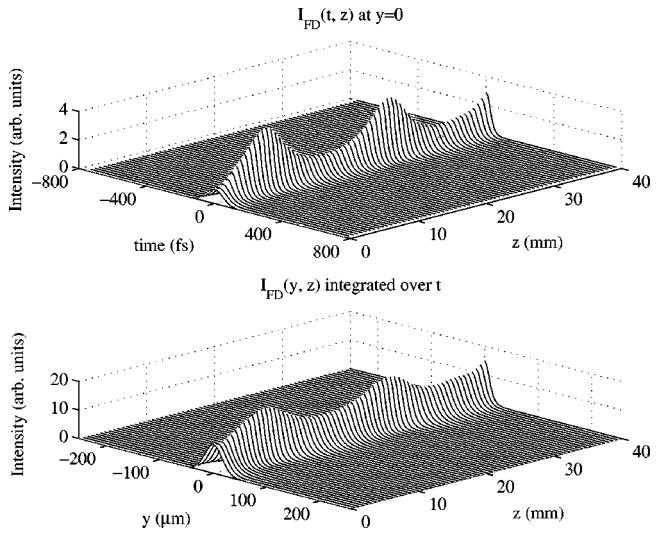

FIG. 4. Simulated FH temporal (upper) and spatial (lower) pulse propagation in $LiIO_3$ with $I=13$ GW/cm^2, $\Delta k=-30\pi/10$ mm, and GVM=0.

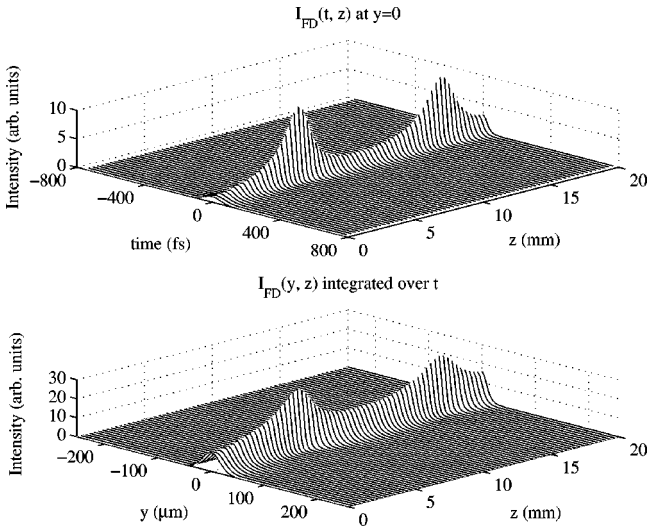

FIG. 5. Simulated FH temporal (upper) and spatial (lower) pulse propagation in $LiIO_3$ with $I=60$ GW/cm^2, $\Delta k=-80\pi/10$ mm, and GVM=0.

In phase-mismatched type-I SHG, GVM distorts the temporal variation of $\Delta\Phi^{\mathrm{NL}}$, which produces a highly nonlinear frequency chirp across the center of a pulse. Thus, it is detrimental to pulse shaping. In previous work on mode locking [43] and pulse compression [44], we developed and confirmed experimentally a way to control the deleterious effects of GVM. With large enough phase mismatch, the cycles of frequency conversion that generate the cascade phase shift occur before the pulses can move away from each other because of GVM. Improved phase-shift ''quality'' comes at the expense of the magnitude, but the reduction of the magnitude is slower than $1/\Delta kL$ in saturation. At least two conversion cycles occur within each L_{GVM} if

$$|\Delta k|\gtrsim 4\pi/L_{\mathrm{GVM}}=4\pi(n_{1g}-n_{2g})/c\tau_0, \qquad (2)$$

and we have found this to be adequate to suppress the deleterious effects of GVM. A similar argument holds for spatial walkoff.

In mode locking and pulse compression, Kerr-like phase shifts $[\Delta\Phi^{\mathrm{NL}}\sim I(t)]$ are desired, so saturation of $\Delta\Phi^{\mathrm{NL}}$ is unnecessary and usually undesirable because it distorts the phase shift near the peak of the pulse. Saturation is essential to the stabilization of STS's, so GVM presents a further restriction in this application: ΔkL cannot be increased indefinitely to accommodate arbitrarily large GVM. An increase of ΔkL by a factor of m, for example, necessitates an increase in intensity by a factor of m^2 to maintain the same degree of saturation, which increases $\Delta\Phi^{\mathrm{NL}}$ by a factor of m. The nonlinear phase shift per characteristic length (L_{DF} or L_{DS}) is proportional to $L_{\mathrm{DS}}/L_{\mathrm{NL}}$. To generate solitons without excessive oscillation (which could lead to instability), this phase shift must be limited to $\Delta\Phi^{\mathrm{NL}}\lesssim\pi$. To reach a moderate degree of saturation, the nonlinear drive Γ^2L^2 must be ~ 2 per conversion cycle, which implies a phase shift per cycle of less than $2/2\pi$. With two conversion cycles per characteristic length, we conclude from Eq. (2) that $L_{\mathrm{DS}}/L_{\mathrm{GVM}}\lesssim 4$ for STS formation. Of course, the intensity must not be allowed to exceed the threshold for collapse due to $\chi^{(3)}$. To summarize: the range of magnitude of ΔkL for which STS's form is bounded below by the need to overcome GVM, and above by the need to avoid excessive nonlinear phase shift.

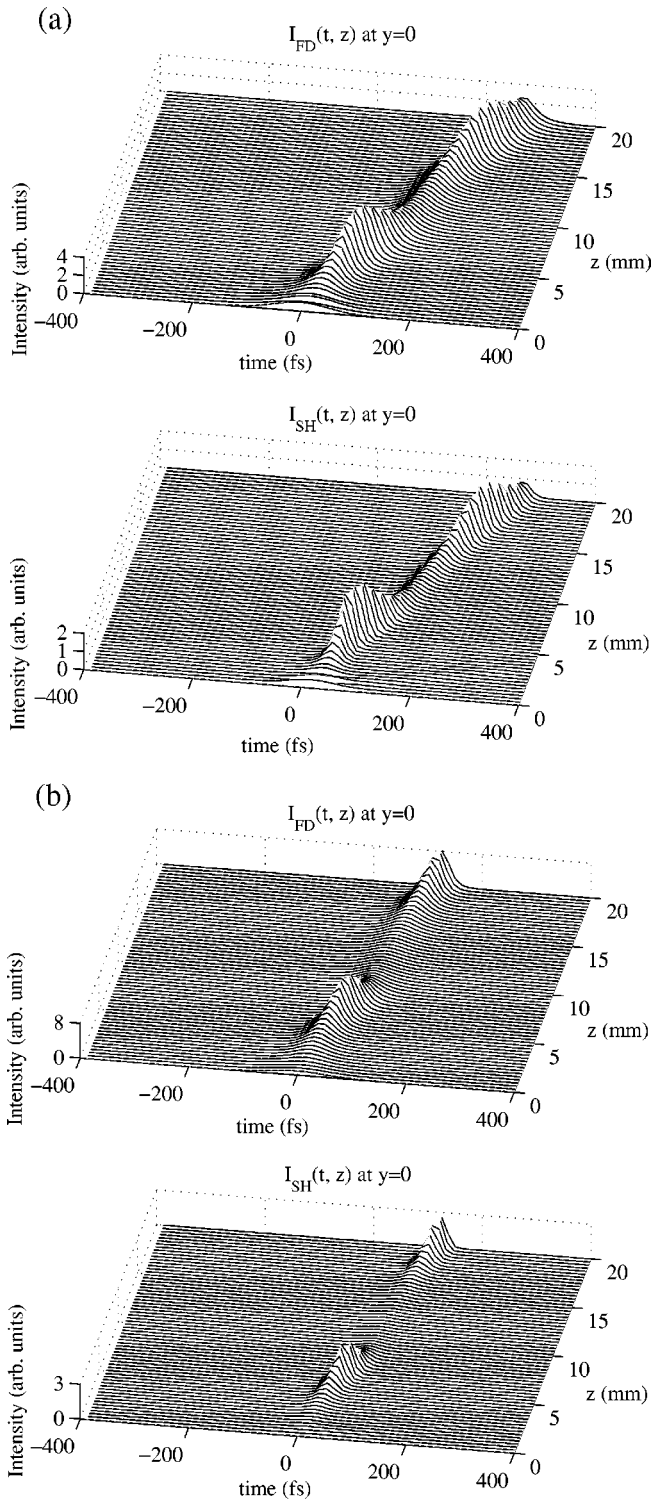

FIG. 6. Simulated propagation of walking solitons with $L_{\mathrm{GVM}}=1$ mm with $\Delta k=-25\pi/10$ mm and $I=13$ GW/cm^2 (a) and with $\Delta k=-50\pi/10$ mm and $I=20$ GW/cm^2 (b).

The process of increasing ΔkL to compensate the effects of GVM is illustrated by the calculated STS of Fig. 6. In the presence of GVM, the mutually-trapped fields will propagate with a velocity between the noninteracting FH and SH group velocities; this is the origin of the terms ''walking'' [23,24]

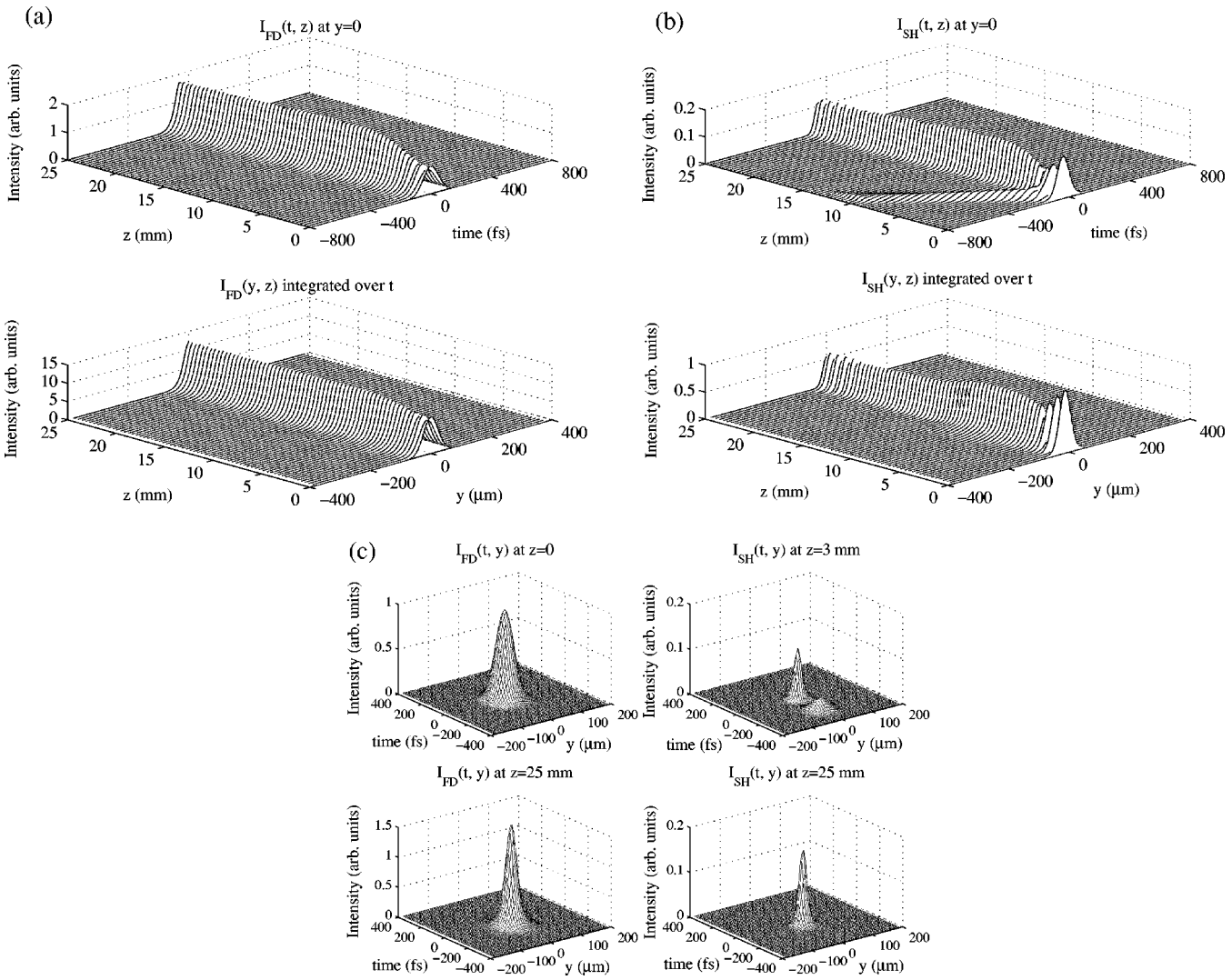

FIG. 7. Simulated stationary STS in BBO: FH (a) and SH (b) pulse propagation with $I=7.5$ GW/cm^2 and $\Delta k=-60\pi/25$ mm. The spatiotemporal profiles of the STS at different propagation lengths are shown in (c).

or ''moving'' [45] solitons. The velocity of a walking soliton is determined by the energy distribution between the FH and SH fields: more energy in the SH field produces a velocity closer to the SH group velocity. As demonstrated in Fig. 6(a), the average speed of the STS is below the FH group velocity, while the instantaneous velocity is directly correlated with the energy distribution at each point. Figure 6(b) shows that increasing the magnitude of ΔkL at fixed GVM brings the walking velocity closer to the FH velocity, as expected since the SH content is reduced. The increase of $|\Delta kL|$ also reduces the energy radiated by the SH field as it evolves to the soliton. Finally, Fig. 6 also shows that larger oscillation occurs at larger $|\Delta kL|$, which is consistent with the argument above regarding saturation.

In the absence of GVM, STS's are represented by real, one-parameter solutions moving at the common group velocity. In the general situation where the group velocities are not matched, soliton solutions are complex (i.e., chirped), and move with a velocity between the FH and SH group velocities. With this additional free parameter, walking solitons form two-parameter families of solutions [23,46].

For experimental studies of STS's with significant GVM, BBO offers some advantages over $LiIO_3$. The GVD and birefringence of BBO allow us to perform experiments at 800 nm with $L_{DS}/L_{GVM}\approx 3$. In linear propagation, the fundamental and harmonic pulses would move away from each other by three times the pulse duration in one characteristic length, and by 15 times the pulse duration in the course of traversing a 25-mm crystal. Other properties of BBO are advantageous for definitive studies of STS's. There is negligible TPA at 400 nm, and a small nonlinear index ($n_2\approx 0.5\times 10^{-15}$ cm^2/W) implies a high threshold for catastrophic collapse due to the Kerr nonlinearity. We will describe experiments done with 17- and 25-mm BBO crystals.

Our criterion for suppressing the effects of GVM yields $|\Delta kL|\gtrsim(40)-60)\,\pi$ for the 17- and 25-mm crystals. We performed numerical calculations with ΔkL in this range, to identify optimal conditions for STS generation in BBO. Stable STS's are generated with $I_0\approx 7.5$ GW/cm^2 and $\Delta kL=-60\pi$ (Fig. 7). The GVM does cause a small amount ($\lesssim 5\%$) of the SH field to radiate away in the first two characteristic lengths [Fig. 7(b)]. However, the subsequent propagation is stable. The STS does walk, as evidenced by the displacement in time relative to the frame of the FH pulse. The small magnitude of the displacement is a conse-

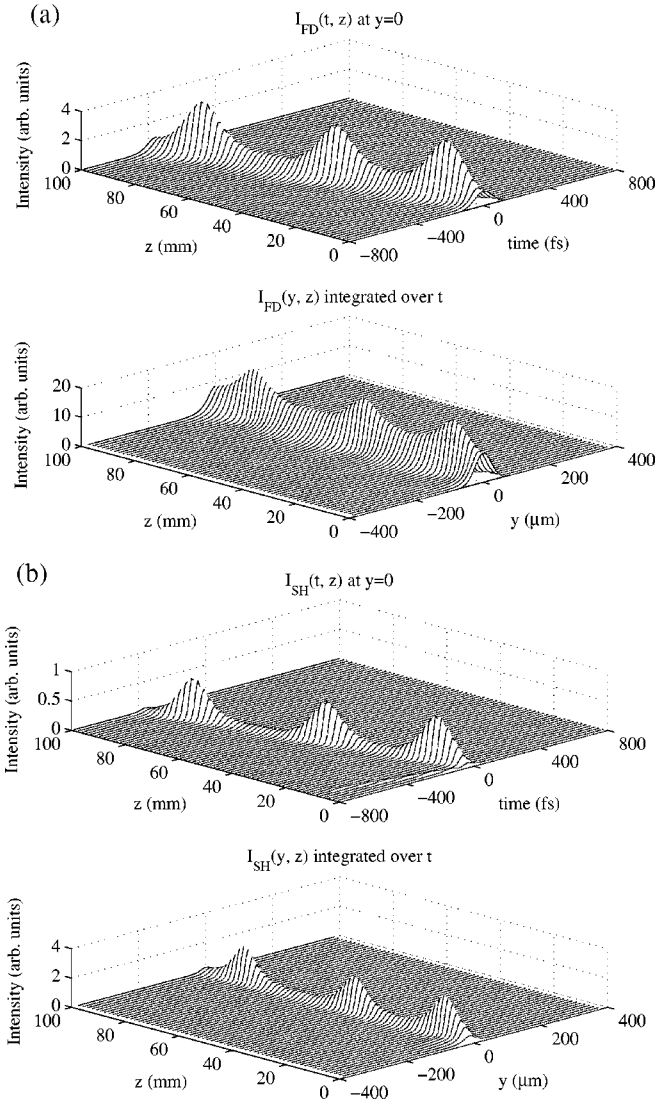

FIG. 8. Simulated oscillatory STS in BBO: FH (a) and SH (b) pulse propagation with $I=9$ GW/cm^2 and $\Delta k=-60\pi/25$ mm.

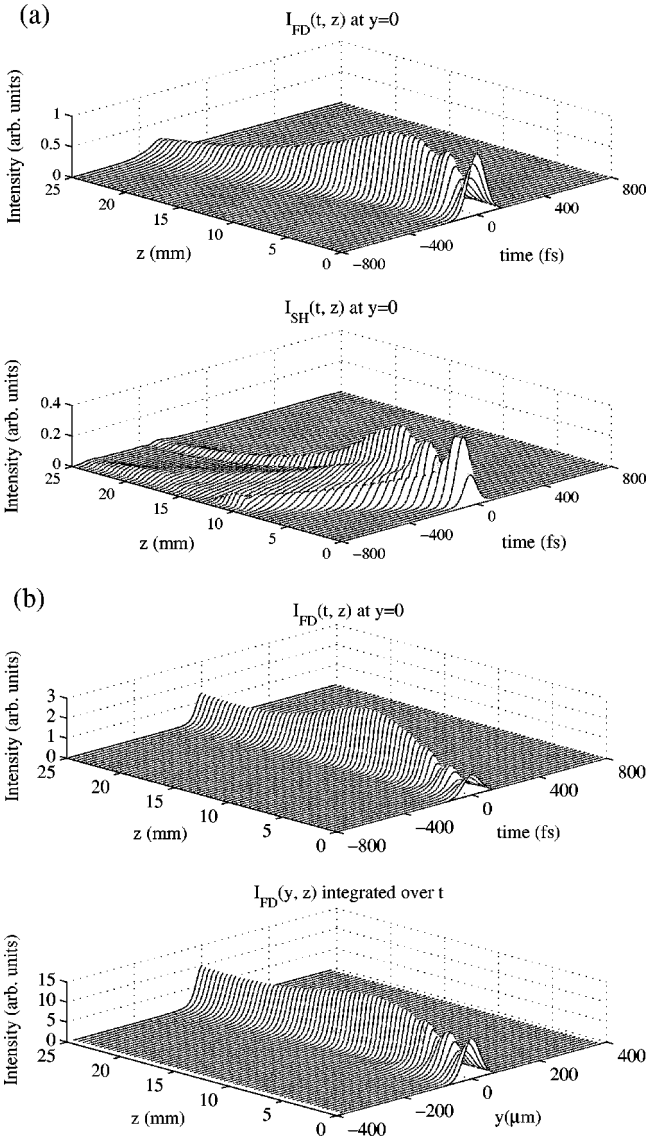

FIG. 9. Calculations of pulse propagation in BBO with $|\Delta kL|$ too small to support mutual trapping of the FH and SH fields (a). The formation of STS's with zero GVM is shown in (b). Conditions for both (a) and (b): $I=4$ GW/cm^2 and $\Delta k=-15\pi/25$ mm.

quence of the large phase mismatch and resulting small SH content in the STS. Calculations with $I_0<5$ GW/cm^2 and $|\Delta kL|<30\pi$ show that the pulse decays, and walks a time interval inversely proportional to ΔkL. Starting from the conditions for stable STS formation, a small increase in the intensity produces a periodic STS (Fig. 8), as was the case with zero GVM.

The consequences of reducing the phase mismatch below the value needed to compensate the effects of GVM are illustrated in Fig. 9(a). With $|\Delta kL|$ reduced to 15π, STS's do not form, and the plot of the SH pulse shows that much energy is lost to strong temporal walkoff of the SH field. Under the same conditions but with zero GVM, STS's do form [Fig. 9(b)].

In experiments with BBO, the diffraction grating is arranged to produce net anomalous GVD of magnitude $|\beta^{(2)}|=1160$ fs^2/mm (430 fs^2/mm) at the FH (SH) frequency, yielding $L_{DS}\approx 4.5$ mm (12 mm) with 120-fs pulses. The resulting $L_{GVM}\approx 1.5$ mm. The beam entering the BBO crystal has diameter 55 μm, which produces $L_{DF}\approx 5$ mm (10 mm) at the FH (SH) frequency. With 17-mm and 25-mm BBO crystals, this allows for propagation over ~ 3.5 and 5.5 characteristic lengths at the FH frequency. We point out that the ratio of the effective FH to SH dispersion lengths is not equal to that of the FH to SH diffraction lengths ($L_{DS1}/L_{DS2} \neq L_{DF1}/L_{DF2}$). Therefore, the space-time profiles of the STS's formed are not perfectly symmetric.

As a control experiment we measured the pulse propagation in the absence of the cascade nonlinearity. With the BBO crystal rotated 90° about the propagation direction to eliminate the quadratic interaction and $I_0\approx 8$ GW/cm^2, the input pulse broadens to 415 fs and 150 μm after propagating through 25 mm of BBO (Fig. 10). These results agree with calculations.

With ΔkL near the theoretical optimum value for STS formation, we measured the pulse duration, spatial profile, and frequency spectrum at the exit face of the 25-mm crystal as functions of the input intensity. The trends observed with $\Delta kL=-60\pi$ are typical. At low intensity (3 GW/cm^2), the pulse duration and spatial profile each broaden by a factor of

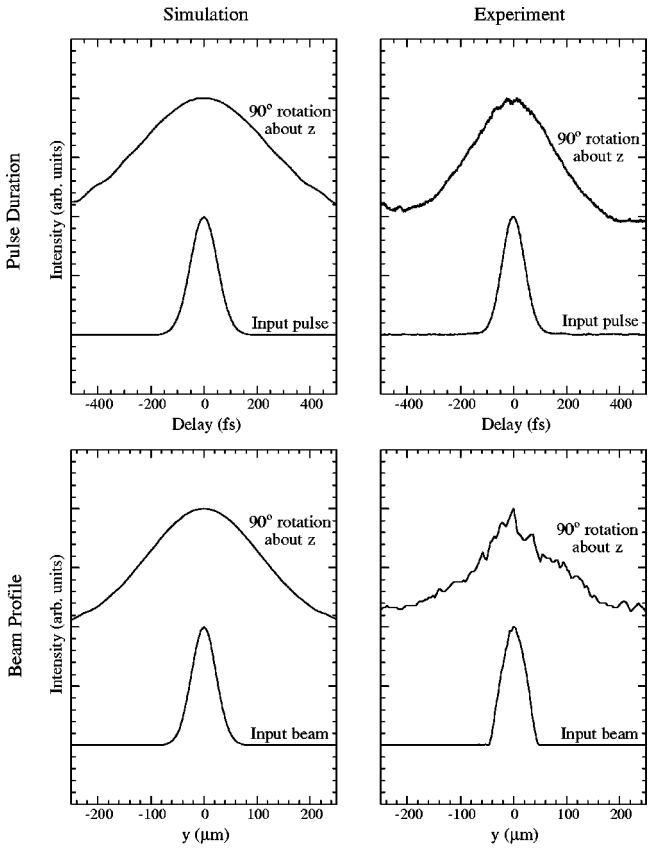

FIG. 10. Temporal and spatial properties of a pulse propagating in the presence of the cubic nonlinearity only. Note: the ''chopped'' appearance of the input spatial profile is an artifact of limited dynamic range of the digital camera.

3–4 (Fig. 11). The nonlinear phase shift and self-focussing arising from the cascade nonlinearity are insufficient to balance dispersion and diffraction. There is no observable change in the pulse spectrum for $I_0 < 3$ GW/cm^2.

Once I_0 reaches 6.5 GW/cm^2, the pulse exiting the BBO crystal begins to narrow in time and space, reaching 110 fs and 70 μm at $I_0 \approx 8$ GW/cm^2. The pulse duration and beam waist agree with the values found in the simulation of STS's under these conditions (calculated traces shown as part of Fig. 11). At this intensity there is a small-amplitude periodic variation of the spatial and temporal profiles. For $I_0 \approx 9$ GW/cm^2 the profiles are similar, but slightly broader than those observed at 8 GW/cm^2. In addition, the spectrum begins to broaden noticeably and develops some structure.

As previously mentioned, the pulse duration decreases with increasing intensity from 360 fs at 3 GW/cm^2 to 110 fs at 9 GW/cm^2 (Fig. 11). Simultaneously, the beam waist narrows from 100 μm at 3 GW/cm^2 to near 70 μm at 7 GW/cm^2. At higher intensity the waist increases again, reaching $\sim$100 μm at 9 GW/cm^2 (Fig. 11). This spatial broadening probably reflects periodic evolution of the STS, i.e., vibration of the internal soliton mode due to slightly exceeding the optimum stationary soliton power at launch.

The pulse propagation observed with $\Delta kL = -60\pi$ and $I_0 \approx 8$ GW/cm^2 is consistent with numerical solutions of STS formation. The hallmark of a soliton is stable propagation, which can only be confirmed directly by measuring the pulse at distinct propagation distances. We replaced the 25-mm

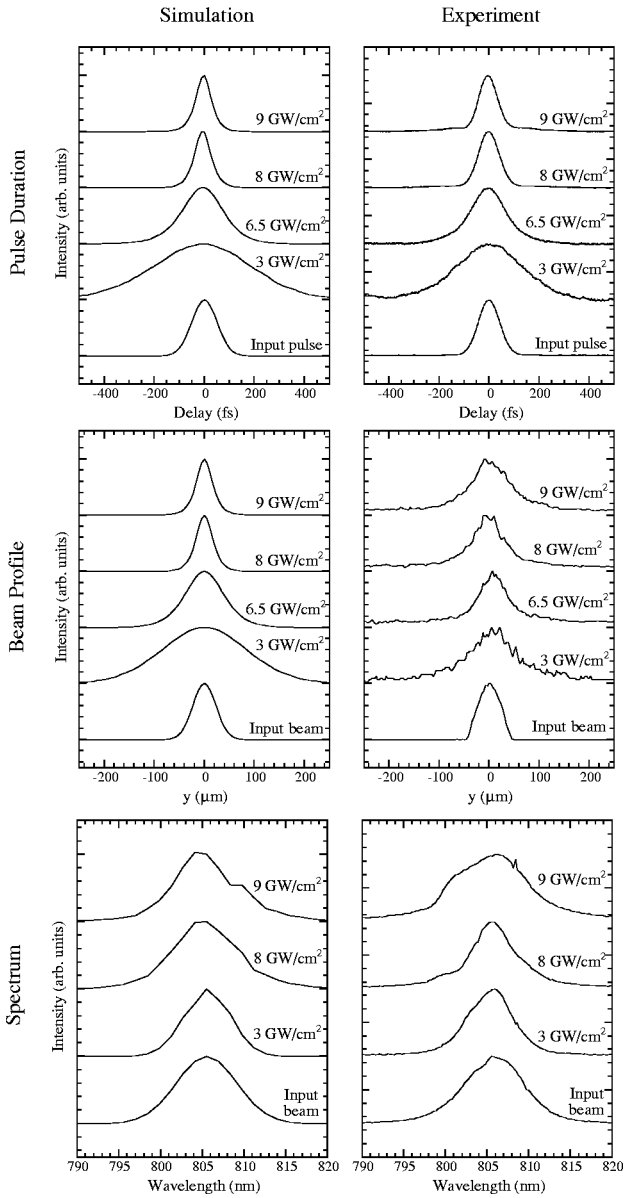

FIG. 11. Temporal, spatial, and spectral profiles of FH pulses at exit face of the crystal with indicated incident intensities at phase mismatch $\Delta kL = -60\pi$. Notice the $\sim$6.5 GW/cm^2 intensity threshold for STS formation and the increase in spectral width above $\sim$8.5 GW/cm^2.

BBO crystal with a piece 17 mm in length, and repeated the above measurements. At intensity 8 GW/cm^2, the output pulse duration is 90 fs [Fig. 12(a)] and beam waist 75 μm [Fig. 12(b)]. These values are close to the pulse parameters after 25-mm propagation. The evolution of the temporal and spatial profiles of Fig. 12 is slightly asymmetric, in contrast to the calculated results (Fig. 8). From Fig. 8, we do see that the simulated FH and SH field intensities oscillate as the pulses propagate, indicating small oscillations in the FH and SH pulse durations and spatial extents which is in qualitative agreement with our temporal [Fig. 12(a)] and spatial [Fig. 12(b)] data.

From the measurements made after propagation through $\sim$3 and $\sim$5 characteristic lengths and the numerical simulations, we conclude that STS's are formed in BBO for parameters in the vicinity of $\Delta kL \approx -60\pi$ and $I_0 \approx 8$ GW/cm^2.

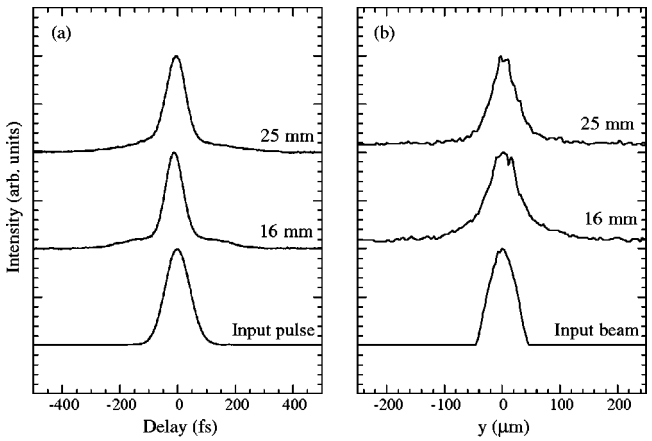

FIG. 12. Experimental temporal (a) and spatial (b) profiles of STS's in BBO with different propagation lengths at $I=8$ GW/cm^2 and $\Delta k=-60\pi/25$ mm.

Because the input pulse is reasonably close to the STS solution, stable mutual trapping occurs in a short propagation distance (~ 1 characteristic length) and the pulse sheds minimal energy as it evolves. After propagation through the BBO crystal, we find that the SH pulse energy is $\sim 2-4\%$ of the input pulse energy, as expected given the large phase mismatch. The total energy is conserved to within a few percent. The absence of two-photon absorption at 400 nm and the small Kerr nonlinearity in BBO make these experiments a nearly ideal realization of the theoretical model [Eq. (1)]. Thus, it seems that BBO provides a better environment than $LiIO_3$ for experimental studies of STS's with fundamental wavelengths around 800 nm. With crystals 30 to 50 mm in length (or multiple shorter crystals), it will also be possible to study nonwalking STS's formed with zero GVM.

The formation of STS's with large GVM demonstrates experimentally the strong coupling of the FH and SH fields in phase-mismatched SHG. These STS's are necessarily chirped, but we do not have direct experimental access to the phase of the electric field. The lack of significant modulation of the pulse spectrum is consistent with the observed small compression of the input pulse. From the time-bandwidth product of the STS's, the chirp cannot be very large. We take this as further confirmation of the reduction of the effects of GVM when the phase mismatch is large. In the future it may be interesting to measure the chirp of the STS's directly, using a technique such as frequency-resolved optical gating [47].

In the initial experimental studies of STS's [35], we investigated pulse propagation with extremely large GVM, $L_{DS}/L_{GVM}\approx 40$. Clear and strong space-time focusing of the input pulse was observed, and based on comparison to numerical simulations we concluded that STS's are produced even with such large GVM. More detailed and extensive calculations with the most accurate material parameters agree with the observed space-time focusing in 10 mm of $LiIO_3$, but also show that the pulse eventually collapses or disperses rather than reaching a stable or periodically stable shape. Thus, the earlier claim of STS formation for $L_{DS}/L_{GVM}\approx 40$ is incorrect; the observed spatio temporal focusing does not produce stable STS's. The experiments described above clearly demonstrate STS formation with

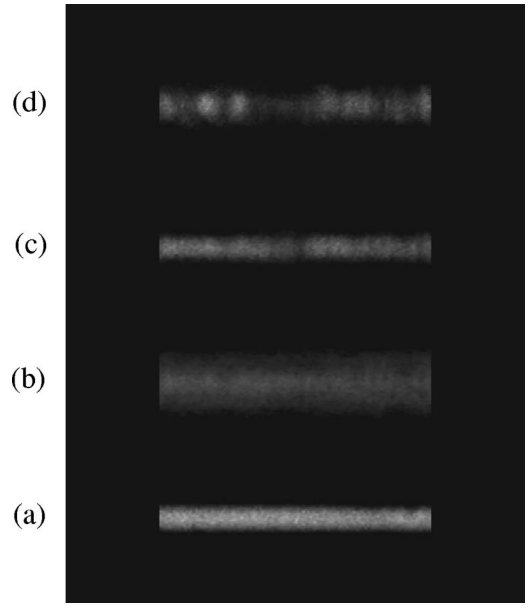

FIG. 13. Spatial profiles of input beam (a) and of FH at exit face of 25-mm BBO with $\Delta kL=-60\pi$ and intensities of 3 GW/cm^2 (b), 8 GW/cm^2 (c), and 9 GW/cm^2 (d). Notice breakup of STS in (c) to filaments in (d).

$L_{DS}/L_{GVM}\approx 3$, and we believe that stable STS's can be generated up to $L_{DS}/L_{GVM}\approx 4$.

VI. LIMITATIONS TO THE STABILITY OF SPATIOTEMPORAL SOLITONS

To this point we have focused on the conditions required to generate STS's. It is important to delineate the range of parameters for which STS's form, and to identify the mechanisms that inhibit STS formation. With the 25-mm BBO crystal, we recorded the output pulse parameters for $-350\pi<\Delta kL<0$ and $0<I_0<20$ GW/cm^2. Typical results obtained along contours of constant ΔkL and I_0 will be presented along with numerical calculations.

We have already shown that dispersive and diffractive propagation is observed at low intensity and large phase mismatch, as expected. With large phase mismatch, the nonlinear phase shift is either (i) too small to support STS's, (ii) large enough but not saturating, or (iii) saturating but too large.

We have also seen (Fig. 11) that at fixed phase mismatch, STS's form above a threshold intensity. That intensity threshold increases with increasing $|\Delta kL|$. At higher intensities, it is possible to observe periodic STS's. However, we also find that the 2D STS's are generally unstable at higher intensities. For example, with $\Delta kL\approx -60\pi$ and $I_0\approx 8.5$ GW/cm^2, the 2D STS's break up into a series of discrete beams along the unfocused (x) dimension. This is illustrated in Fig. 13. A similar filamentation of 1D spatial solitons was reported by Fuerst and co-workers, and attributed to transverse instability (TI) [48]. To investigate this possible explanation, we performed full 3D numerical simulations with a small amount (up to $\sim 4\%$) of random intensity variation added to the incident beam along the x direction. Filamentation of the 2D STS's similar to that observed experimentally occurs in the simulation. The experimental intensity depen-

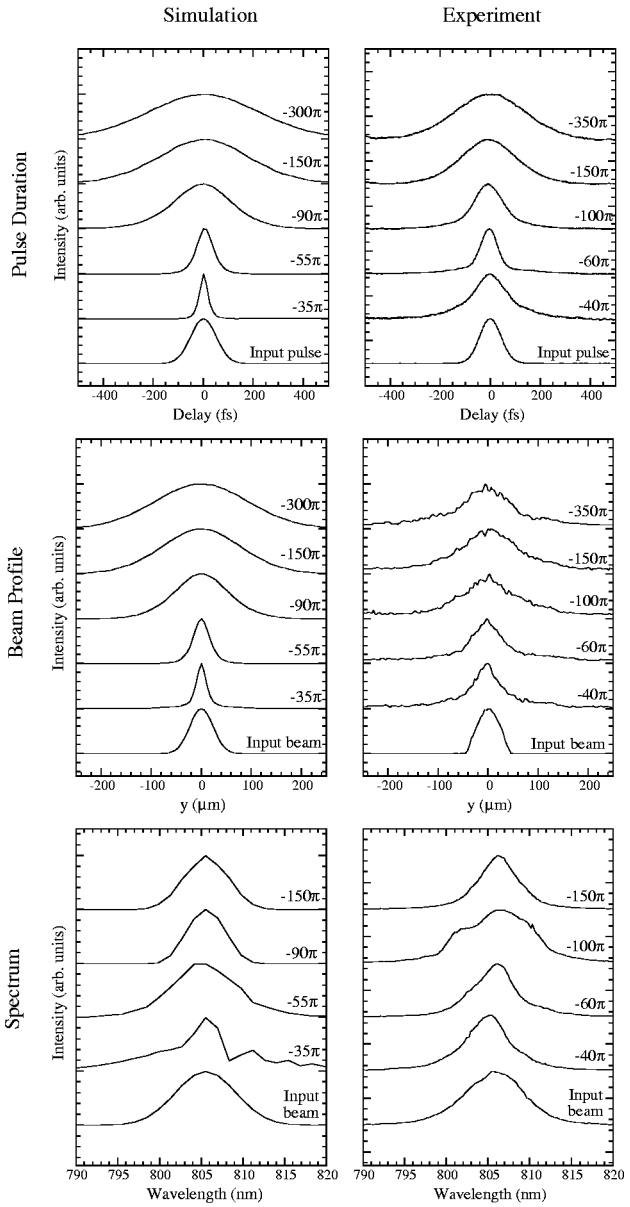

FIG. 14. Temporal, spatial, and spectral profiles of FH pulses at exit face of the crystal with indicated phase mismatches at intensity $I=8$ GW/cm^2. Notice the increase in spectral width for $-100\pi < \Delta kL < -75\pi$.

dence of the spatial frequency of the filaments agrees qualitatively with theoretical predictions for TI-induced breakup [49]. Numerical simulations also show similar qualitative trends. Therefore, we attribute the filamentation to TI. The use of angular dispersion in our experiment should presumably preclude the formation of full 3D STS's: as the filaments propagate, their constituent wavelengths are spread spatially by the angular dispersion. To verify this, we combined the 25- and 17-mm BBO crystals and studied the propagation of the filaments over longer lengths. Initial observations show x dimension broadening of the filaments by an amount commensurate with the angular dispersion required for APM. Hence the angular dispersion influences the propagation of the filaments following breakup, but does not impede the TI-induced breakup itself. A more detailed treatment, along with a discussion of other interesting aspects of

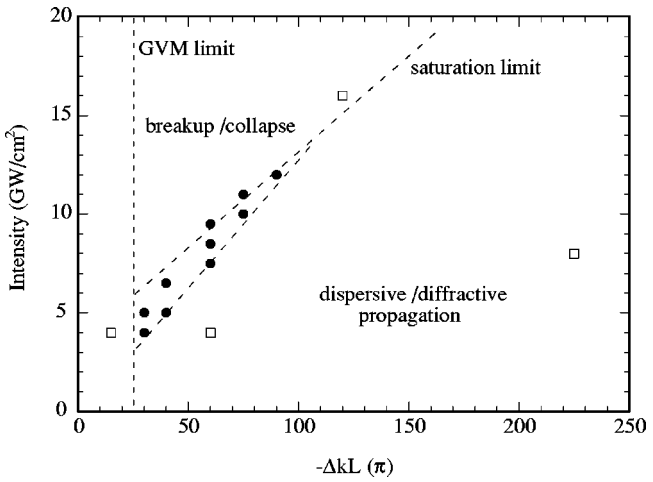

FIG. 15. Stability map for formation of STS's. Solid circles indicate locations of STS formation and open squares indicate locations where STS's do not form. Regions are qualitative and experiment specific.

this mechanism for destabilizing the 2D STS's, will be presented separately [50].

When the beam breaks into filaments, the intensity increases slightly, and the propagation changes from one dimensional to two dimensional in space. The filaments therefore have a greater tendency toward self-focussing collapse via the Kerr nonlinearity. Collapse is manifested experimentally by strong spatial distortions of the output beam: some filaments blur and spread spatially, which indicates strong focusing of the beam within the crystal. The spectrum of these collapsed filaments broadens significantly and develops some structure (Fig. 11). For $\Delta kL \approx -60\pi$ collapse is observed for $I_0 > 8.5$ GW/cm^2.

Varying the phase mismatch while maintaining fixed intensity produces a qualitatively similar trend. As an example, measurements made with $I_0 \approx 8.5$ GW/cm^2 are shown in Fig. 14. For $|\Delta kL| \gtrsim 100\pi$, the cascade phase shift is small, so the pulse broadens in time and space. As the phase mismatch is reduced in magnitude, the pulse narrows in space and time, and then broadens in time at very small phase mismatch. The pulse duration (beam waist) reaches a minimum of 95 fs (70 μm) at $\Delta kL = -60\pi$, and then goes to 180 fs ($\sim$60 μm) at $\Delta kL = -40\pi$. Through this range the pulse spectra are single peaked, but broaden by a factor of ~ 2 over the range $-100\pi < \Delta/kL < -75\pi$ before narrowing at small phase mismatch. If we adjust ΔkL closer to zero starting from conditions that produce stable STS's, we again observe filamentation of the beam. These results largely agree with calculations (Fig. 14). The apparent discrepancy in pulse duration between the calculations and experiment for $-60\pi < \Delta kL < -40\pi$ is due to the space-time asymmetry imposed by GVM and TI-induced breakup; the filaments attract energy from their surroundings. This is a full three-dimensional process and is thus not treated correctly by two-dimensional simulations.

The breakup of the STS's due to TI was also observed in experiments with $LiIO_3$. For a given phase mismatch, the threshold intensity for filamentation is somewhat higher than in BBO. We believe that this is another consequence of the TPA at 400 nm in $LiIO_3$. The higher threshold intensity for

TI in $LiIO_3$ permits the study of STS formation over a wider range of intensities than is possible with BBO.

Generally, 2D STS's are theoretically unstable against collapse due to the Kerr nonlinearity or the transverse instability. For large enough phase mismatch (or high enough intensity), the $\chi^{(3)}$ nonlinearity will dominate, and self-focusing collapse is expected. The critical power for one-dimensional self-focusing by the Kerr nonlinearity is ~ 100 GW/cm^2 in BBO. Under the conditions of the experiments described here ($I_0 \leqslant 10$ GW/cm^2), the Kerr phase shift is $<10\%$ of the cascade phase shift. Thus, Kerr self-focusing is not a major impediment to the production of 2D STS's. However, at large phase mismatch it can contribute to collapse of the filaments that arise from the transverse instability. For $-100\pi < \Delta kL < -40\pi$, the cascade nonlinearity dominates the Kerr nonlinearity.

Finally, for $-40\pi < \Delta kL < 0$, STS's are not observed regardless of intensity (for intensities below the damage threshold of BBO). This boundary is roughly consistent with our criterion [Eq. (2)] for the phase mismatch needed to suppress the effects of GVM. Closer to phase matching, the FH and SH pulses may move apart in time before mutual trapping can take place.

A map of the values of intensity and phase mismatch that produce distinct pulse evolutions can be compiled from measurements similar to those described above, and such a map is shown in Fig. 15. While the general features are representative, the details are specific to other experimental factors, such as the GVM and the uniformity and aspect ratio of the input beam. The map is therefore a qualitative guide to STS formation under general conditions.

The production of solitons in the presence of quadratic and cubic nonlinearities has been treated by several groups of researchers [51–53]. The region of the ΔkL-I_0 plane over which STS's form has the shape expected theoretically for $\Delta kL < 0$ [52]. The calculations neglect dispersion, and thus cannot predict the boundary that arises from GVM. Theoretically, it is also possible to observe STS's with a self-defocusing Kerr nonlinearity partially compensating the cascade nonlinearity to produce net self-focusing [54].

VII. CONCLUSION

The experimental work presented here outlines the conditions of input-pulse intensity and phase mismatch under which STS's are produced, and these agree generally with theoretical predictions and particularly with numerical calculations of the pulse propagation. Theoretically predicted walking solitons exist experimentally for large group-velocity mismatch ($L_{DS}/L_{GVM} \approx 3$), and we believe that somewhat larger group-velocity mismatch can be tolerated. Transverse instability significantly limits the conditions under which STS's can be observed experimentally, although it is possible that this can be managed to some extent by choice of the input-beam shape. On the positive side, the instability may provide an appealing way to generate fully confined 3D STS's. Future work will address this issue.

ACKNOWLEDGMENTS

This work was supported by the National Science Foundation under Award No. ECS-9612255, the National Institutes of Health under Award No. RR10075, and the Cornell Theory Center. The authors thank M. Segev, P. Di Trapani, B. Malomed, J. Pérez Torres, and L. Torner for valuable discussions, and A. Gaeta for the use of the digital camera.

[1] A. Hasegawa and F. Tappert, Appl. Phys. Lett. **23**, 142 (1973).
[2] L. F. Mollenauer, R. H. Stolen, and J. P. Gordon, Phys. Rev. Lett. **45**, 1095 (1980).
[3] V. E. Zakharov and A. M. Rubenchik, Zh. Éksp. Teor. Fiz. **65**, 997 (1973) [Sov. Phys. JETP **38**, 494 (1974)].
[4] A. Barthelemy, S. Maneuf, and C. Froehly, Opt. Commun. **55**, 201 (1985).
[5] J. E. Bjorkholm and A. Ashkin, Phys. Rev. Lett. **32**, 129 (1974).
[6] J. S. Aitchison, A. M. Weiner, Y. Silberberg, M. K. Oliver, J. L. Jackel, D. E. Leaird, E. M. Vogel, and P. W. E. Smith, Opt. Lett. **15**, 471 (1990).
[7] M. Segev, B. Crosignani, A. Yariv, and B. Fischer, Phys. Rev. Lett. **68**, 923 (1992).
[8] G. C. Duree, J. L. Schultz, G. J. Salamo, M. Segev, A. Yariv, B. Crosignani, P. DiPorto, E. J. Sharp, and R. R. Neurgaonkar, Phys. Rev. Lett. **71**, 533 (1993).
[9] N. R. Belashenkov, S. V. Gagarskii, and M. V. Inochkin, Opt. Spektrosk. **66**, 1383 (1989) [Opt. Spectrosc. **66**, 806 (1989)].
[10] H. J. Bakker, P. C. M. Planken, L. Kuipers, and A. Lagendijk, Phys. Rev. A **42**, 4085 (1990).
[11] R. DeSalvo, D. J. Hagan, M. Sheik-Bahae, G. Stegeman, E. W. Van Stryland, and H. Vanherzeele, Opt. Lett. **17**, 28 (1992).
[12] A. A. Kanashov and A. M. Rubenchik, Physica D **4**, 1222 (1981).
[13] Y. N. Karamzin and A. P. Sukhorukov, Zh. Éksp. Teor. Fiz. **68**, 834 (1975) [Sov. Phys. JETP **41**, 414 (1975)].
[14] C. R. Menyuk, R. Schiek, and L. Torner, J. Opt. Soc. Am. B **11**, 2434 (1994).
[15] A. V. Buryak and Y. S. Kivshar, Opt. Lett. **19**, 1612 (1994).
[16] L. Torner, C. R. Menyuk, and G. I. Stegeman, Opt. Lett. **19**, 1615 (1994).
[17] S. K. Turitsyn, Pis'ma Zh. Éksp. Teor. Fiz. **61**, 458 (1995) [JETP Lett. **61**, 469 (1995)].
[18] L. Berge, V. K. Mezentsev, J. J. Rasmussen, and J. Wyller, Phys. Rev. A **52**, R28 (1995).
[19] L. Torner, W. E. Torruellas, G. I. Stegeman, and C. R. Menyuk, Opt. Lett. **20**, 1952 (1995).
[20] A. De Rossi, S. Trillo, A. V. Buryak, and Y. S. Kivshar, Opt. Lett. **22**, 868 (1997).
[21] D. E. Pelinovsky, A. V. Buryak, and Y. S. Kivshar, Phys. Rev. Lett. **75**, 591 (1995).
[22] C. Etrich, U. Peschel, F. Lederer, B. A. Malomed, and Y. S. Kivshar, Phys. Rev. E **54**, 4321 (1996).
[23] L. Torner, D. Mazilu, and D. Mihalache, Phys. Rev. Lett. **77**, 2455 (1996).
[24] D. Mihalache, D. Mazilu, L.-C. Crasovan, and L. Torner, Opt. Commun. **137**, 113 (1997).
[25] P. D. Drummond and H. He, Phys. Rev. A **56**, R1107 (1997).

[26] W. E. Torruellas, Z. Wang, D. J. Hagan, E. W. Van Stryland, G. I. Stegeman, L. Torner, and C. R. Menyuk, Phys. Rev. Lett. **74**, 5036 (1995).
[27] P. Di Trapani, D. Caironi, G. Valiulis, A. Dubietis, R. Danielius, and A. Piskarskas, Phys. Rev. Lett. **81**, 570 (1998).
[28] E. A. Kuznetsov, A. M. Rubenchik, and V. E. Zakharov, Phys. Rep. **142**, 105 (1986); J. J. Rasmussen and K. Rypdal, Phys. Scr. **33**, 481 (1986).
[29] Y. Silberberg, Opt. Lett. **15**, 1282 (1990).
[30] A. Braun, G. Korn, X. Liu, D. Du, J. Squier, and G. Mourou, Opt. Lett. **20**, 71 (1995).
[31] D. E. Edmundson and R. H. Enns, Opt. Lett. **17**, 586 (1992).
[32] H. He, M. J. Werner, and P. D. Drummond, Phys. Rev. E **54**, 896 (1996).
[33] B. A. Malomed, P. Drummond, H. He, A. Berntson, D. Anderson, and M. Lisak, Phys. Rev. E **56**, 4725 (1997).
[34] D. Mihalache, D. Mazilu, B. A. Malomed, and L. Torner, Opt. Commun. **152**, 365 (1998).
[35] X. Liu, L. J. Qian, and F. W. Wise, Phys. Rev. Lett. **82**, 4631 (1999).
[36] O. E. Martinez, IEEE J. Quantum Electron. **25**, 2464 (1989).
[37] G. Valiulis, A. Dubietis, R. Danielius, D. Caironi, A. Visconti, and P. Di Trapani, J. Opt. Soc. Am. B **16**, 722 (1999).
[38] D. Mihalache, D. Mazilu, J. Dorring, and L. Torner, Opt. Commun. **159**, 129 (1999).
[39] K. A. Stankov, Opt. Lett. **14**, 359 (1989).
[40] M. Zavelani-Rossi, G. Cerullo, and V. Magni, IEEE J. Quantum Electron. **34**, 61 (1998).
[41] O. Albert and J. Etchepare, Opt. Commun. **154**, 345 (1998).
[42] I. Kang, T. Krauss, and F. W. Wise, Opt. Commun. **22**, 1077 (1997).
[43] L. J. Qian, X. Liu, and F. W. Wise, Opt. Lett. **24**, 166 (1999).
[44] X. Liu, L. J. Qian, and F. W. Wise, Opt. Lett. **24**, 1778 (1999).
[45] C. Etrich, U. Peschel, F. Lederer, and B. A. Malomed, Phys. Rev. E **55**, 6155 (1997).
[46] D. Mihalache, D. Mazilu, B. A. Malomed, and L. Torner, Opt. Commun. **169**, 341 (1999).
[47] R. Trebino and D. J. Kane, J. Opt. Soc. Am. A **10**, 1101 (1993); B. Kohler, V. V. Yakovlev, K. R. Wilson, J. Squier, K. W. DeLong, and R. Trebino, Opt. Lett. **20**, 483 (1995).
[48] R. A. Fuerst, D.-M. Baboiu, B. Lawrence, W. E. Torruellas, G. I. Stegeman, S. Trillo, and S. Wabnitz, Phys. Rev. Lett. **78**, 2756 (1997).
[49] D. V. Skryabin and W. J. Firth, Opt. Commun. **148**, 79 (1998).
[50] X. Liu, K. Beckwitt, and F. Wise (unpublished).
[51] O. Bang, Y. S. Kivshar, A. V. Buryak, A. De Rossi, and S. Trillo, Phys. Rev. E **58**, 5057 (1998).
[52] L. Berge, O. Bang, J. J. Rasmussen, and V. K. Mezentsev, Phys. Rev. E **55**, 3555 (1997).
[53] A. De Rossi, G. Assanto, S. Trillo, and W. E. Torruellas, Opt. Commun. **150**, 390 (1998).
[54] O. Bang, Y. S. Kivshar, and A. V. Buryak, Opt. Lett. **22**, 1680 (1997).